The Planetary Science Journal, 1:78 (13pp), 2020 December https://doi.org/10.3847/PSJ/abcaf9

Recovery and Validation of Venus Ionospheric Electron Density Profiles from Pioneer Venus Orbiter Radio Occultation Observations

Paul Withers[1,2,4], Kerry Hensley[1], Marissa F. Vogt[2], and Jacob Hermann[3]
[1] Astronomy Department, Boston University, 725 Commonwealth Avenue, Boston, MA 02215, USA
[2] Center for Space Physics, Boston University, 725 Commonwealth Avenue, Boston, MA 02215, USA
[3] University of Colorado, Boulder, CO 80309, USA
Received 2020 July 9; revised 2020 November 11; accepted 2020 November 12; published 2020 December 17

Abstract

The Pioneer Venus Orbiter radio occultation experiment acquired vertical profiles of electron density in the ionosphere of Venus. These profiles were not readily accessible to researchers. Here we report the recovery and validation of a set of electron density profiles from Pioneer Venus Orbiter. More than 200 profiles spanning solar zenith angles of 30°–170° were deemed acceptable for scientific analysis. These profiles sample solar minimum, moderate, and maximum conditions. The profiles are publicly available and ready for use in scientific investigations of the ionosphere of Venus and related topics.

Unified Astronomy Thesaurus concepts: Venus (1763)

1. Introduction

Pioneer Venus was one of NASA's most successful planetary science missions (Colin 1977; Mutch 1980; Hunten et al. 1983; Bougher et al. 1997). Its orbiter and atmospheric entry probes conducted the first comprehensive study of the atmosphere of another planet. Pioneer Venus Orbiter (PVO), which operated at Venus from 1978 to 1992, determined the composition, structure, and energetics of the neutral upper atmosphere and ionosphere of Venus. It also determined how the plasma environment around Venus is produced by the interaction of the solar wind with Venus.

PVO carried a radio occultation investigation (ORO, led by the late Arv Kliore of JPL) that produced two main data products: vertical profiles of ionospheric electron density and vertical profiles of neutral atmospheric temperature and pressure (Kliore et al. 1979a, 1979b; Berman & Ramos 1980; Kliore & Patel 1980, 1982; Cravens et al. 1981; Woo et al. 1982, 1989; Newman et al. 1984; Kliore 1985; Kliore & Mullen 1989, 1990; Zhang et al. 1990; Brace & Kliore 1991; Kliore & Luhmann 1991; Kliore et al. 1991; Woo & Kliore 1991; Kliore 1992).

Raw radio occultation data from PVO are archived at https://pds-ppi.igpp.ucla.edu/archive1/PV04_0001/ to PV04_0066/. Unfortunately, the high-level data products of the PVO radio occultation investigation, the ionospheric and neutral atmospheric profiles, are not archived at the NASA Planetary Data System (PDS). These ionospheric profiles are not currently available to the scientific community in a digital format. As part of a wide-ranging program to acquire and archive ionospheric electron density profiles from radio occultation experiments (Withers et al. 2015; Dalba & Withers 2019; Withers et al. 2020), we conducted a search for the PVO radio occultation ionospheric electron density profiles. The aim of this article is to report the successful recovery and validation of many of these profiles. The recovered profiles and comprehensive documentation are available at https://hdl.handle.net/2144/41269. In 2020 August, this material was delivered to the PDS for review and archiving.

The structure of this document is as follows. Section 2 outlines the scientific value of radio occultation profiles at Venus. Section 3 assesses the availability of ionospheric profiles at Venus from other experiments. Section 4 describes the availability of data from PVO radio occultations. Section 5 validates the ionospheric profiles by comparing National Space Science Data Center (NSSDC) and graphical ionospheric profiles for the same occultation. Section 6 reports an overview of the ionospheric profiles. Section 7 presents the conclusions of this project.

2. The Scientific Value of Radio Occultation Electron Density Profiles at Venus

Venus and Earth began as twins, possessing near-identical sizes and densities, yet a less Earth-like environment than present-day Venus is hard to imagine. Venus is hellishly hot, devoid of oceans, apparently lacking plate tectonics, and immersed in a thick, reactive atmosphere. How, why, and when did the evolutionary paths of Earth and Venus diverge?

Such questions prompted a sustained program of Soviet exploration and the NASA Pioneer Venus and Magellan missions. More recently, ESA's Venus Express orbiter operated successfully at Venus from 2006 to 2014 and Japan's Akatsuki/Planet-C Venus Climate Orbiter mission entered orbit in 2015. Although NASA has not launched a mission to Venus for 30 years, the US planetary science community maintains a strong interest in the continued exploration of Venus, as demonstrated by the activities of VEXAG, the NASA-chartered Venus Exploration Analysis Group, and the regular submission of strongly rated Venus mission proposals to the NASA Discovery program. For example, two Venus mission concepts (VERITAS and DAVINCI) were selected for Phase A studies in the NASA Discovery program in 2015 and 2020.

Radio occultation electron density profiles at Venus are relevant to several of the 10 priority questions identified by the 2011 Planetary Science Decadal Survey:

[4] Corresponding author.

5. Did Mars or Venus host ancient aqueous environments conducive to early life? (for example, what is the role of the ionosphere in the present-day loss of volatiles to space?)

10. How have the myriad chemical and physical processes that shaped the solar system operated, interacted, and evolved over time? (for example, how do the ionosphere and neutral atmosphere of Venus interact?)

Examples of focused science questions that can be answered using the PVO radio occultation data and that are aligned with the strategic goals of NASA's Planetary Science Division include the following:

1. Can features in the radio occultation electron density profiles be connected to changes in ionospheric composition or temperature with altitude, which were measured by PVO's in situ instruments (Bauer et al. 1985)?
2. Measurements of electron densities in the ionosphere of Venus by three in situ PVO instruments are inconsistent (Brace et al. 1997). With which in situ data sets are radio occultation electron density profiles consistent?

3. Availability of Electron Density Profiles at Venus from Other Experiments

The only vertical profiles of the electron density held by the PDS or related archives that encompass the main ionospheric peak are 29 profiles from Venera 15/16 (https://pds-ppi.igpp.ucla.edu/data/V15_V16-V-ROE-5-OCC-ELECTRON-DENS-V1.0/), whose delivery to the PDS we coordinated in 2010. Ionospheric data from PVO's in situ instruments are available from the PDS PPI node, but they do not approach within two scale heights of the ionospheric peak, which is the region of greatest interest. In the modern era, access to several hundred ionospheric electron density profiles from the Venus Express radio occultation experiment can be requested from the experimenters (http://www.radio-science.eu/?page_id=746&lang=en), but these profiles have not yet been formally archived (Häusler et al. 2006; Pätzold et al. 2007). Several ionospheric electron density profiles from the Magellan and Akatsuki radio occultation experiments have been reported in publications (Jenkins et al. 1994; Jenkins 1998; Imamura et al. 2017) but have not been archived.

The recovery of electron density profiles from the PVO radio occultation investigation would significantly increase the number of such profiles available for scientific analysis. This would also enable studies of temporal variations in the ionosphere (e.g., solar cycle).

4. Availability of Data from PVO Radio Occultations

Many observations were acquired by PVO ORO. Kliore & Luhmann (1991) describe 148 day-side ionospheric profiles, and Zhang et al. (1990) describe roughly 125 night-side ionospheric profiles. PVO's valuable radio occultation ionospheric profiles were never archived at the PDS nor disseminated outside the team. The last publications to use these data appeared over 20 years ago (Brace et al. 1997; Fox & Kliore 1997). These data have never been available for comparison to Venus Express or Akatsuki observations, nor have they been available for comparative studies of the ionospheres of Venus and Mars, which are very similar, since the reinvigoration of Mars science that began with Mars Global Surveyor.

As part of a wide-ranging program to acquire and archive ionospheric electron density profiles from radio occultation experiments, we conducted a search for PVO's radio occultation ionospheric profiles. The PDS does hold the raw data (Original Data Records, ODRs) from PVO's radio occultations (https://pds-ppi.igpp.ucla.edu/archive1/PV04_0001/ to PV04_0066/). However, these raw data are very raw, processing them would require a great deal of ancillary information that may not exist, and any effort to process them would be long, hard, and uncertain of success.

The NSSDC provided us with a copy of data set PSPA-00345 (http://nssdc.gsfc.nasa.gov/nmc/datasetDisplay.do?id=PSPA-00345). This data set, which was previously identified as 78-051A-20A, included a set of UNIVAC binary files and one PDF document (hereafter PSPA-00345.pdf). As described more fully in Appendix A and the documentation available at https://hdl.handle.net/2144/41269, 93 electron density profiles were recovered from this data set. Furthermore, figures in Kliore & Luhmann (1991) contain 90 profiles and figures in Kliore (1992) contain 64 profiles. As described more fully in Appendix A and the documentation available at https://hdl.handle.net/2144/41269, 154 representations of 134 profiles were recovered from these sources. We label profiles recovered from the NSSDC data set as "NSSDC" profiles and profiles recovered from published figures as "graphical" profiles.

It was necessary to generate additional ancillary information to support the analysis and interpretation of these ionospheric observations, including the time of the observation, Venus-centric latitude, Venus-centric east longitude, local solar time, and whether the observation was ingress or egress. As described more fully in Appendix A and the documentation available at https://hdl.handle.net/2144/41269, we generated this information using SPICE.

5. Comparison of NSSDC and Graphical Ionospheric Profiles for the Same Occultation

Comparison of NSSDC and graphical profiles for the same occultation provides insight into errors that may have been introduced in the graphical recovery process. However, we caution that the PVO experimenters may have used different versions of a profile for NSSDC delivery and for publication in articles. For example, the data-processing pipeline may have evolved between the generation of one version and the generation of the other version. Despite this caveat, comparison of duplicate profiles remains useful.

Figures 7(a) and 8(a) of Kliore (1992) each contain 11 profiles from the time period covered by the NSSDC profiles. NSSDC representations exist for 9 of the 11 profiles in Figure 7(a) of Kliore (1992) and for 3 of the 11 profiles in Figure 8(a) of Kliore (1992). Table 1 lists these profiles, the rms difference in electron density values, and solar zenith angle from SPICE. Individual profiles are identified by labels. For example, the graphical profile obtained from the third profile in Figure 5(b) of Kliore & Luhmann (1991) is labeled as k91_5b_03. A different convention is applied to the NSSDC profiles. An example of a label for an NSSDC profile is pvoro_nssdc_eden_0020_n_cl_d_v01_r00.tab, where "pvoro" indicates the PVO ORO experiment, "nssdc" indicates an NSSDC profile, "eden" indicates an electron density profile, "0020"' indicates orbit 20, "n" indicates ingress ("x" if egress), "cl" indicates a closed-loop observation ("ol" if open loop), and "d" indicates a differential Doppler observation ("s" if *S* band, "x" if *X* band).

Table 1
Ionospheric Electron Density Profiles for which Both NSSDC and Graphical Representations Exist

Graphical	NSSDC	rms Difference (cm^{-3})	Solar Zenith Angle (deg)
k92_7a_01	pvoro_nssdc_eden_0020_n_cl_d_v01_r00.tab	6.5×10^3	90.72
k92_7a_02	pvoro_nssdc_eden_0022_n_cl_d_v01_r00.tab	1.2×10^4	91.51
k92_7a_03	pvoro_nssdc_eden_0026_n_cl_d_v01_r00.tab	4.0×10^3	93.17
k92_7a_04	pvoro_nssdc_eden_0029_n_cl_d_v01_r00.tab	3.5×10^3	94.53
k92_7a_05	pvoro_nssdc_eden_0031_n_cl_d_v01_r00.tab	8.7×10^3	95.37
k92_7a_07	pvoro_nssdc_eden_0033_n_cl_d_v01_r00.tab	3.4×10^3	96.42
k92_7a_08	pvoro_nssdc_eden_0034_n_cl_d_v01_r00.tab	4.3×10^3	96.92
k92_7a_09	pvoro_nssdc_eden_0035_n_cl_d_v01_r00.tab	6.2×10^3	97.47
k92_7a_11	pvoro_nssdc_eden_0037_n_cl_d_v01_r00.tab	3.5×10^3	98.53
k92_8a_01	pvoro_nssdc_eden_0053_n_cl_d_v01_r00.tab	3.9×10^3	108.57
k92_8a_02	pvoro_nssdc_eden_0055_n_cl_d_v01_r00.tab	1.5×10^3	110.32
k92_8a_07	pvoro_nssdc_eden_0045_x_cl_d_v01_r00.tab	3.6×10^3	146.42

Further details on these labeling conventions are provided in the documentation available at https://hdl.handle.net/2144/41269.

Panel (a) of Figure 1 shows profiles for the ingress occultation on orbit 20. The basic shapes of the two representations are similar, although slight offsets are apparent.

Panel (b) of Figure 1 shows profiles for the ingress occultation on orbit 22. The two representations are sufficiently different that we considered whether we had misidentified an observation. We examined other NSSDC profiles at similar solar zenith angles and dates to see if a better match existed, but without appreciable improvement. The basic shapes of the two representations are similar, however, even though substantial offsets in electron density are present.

Panel (c) of Figure 1 shows profiles for the ingress occultation on orbit 26. These two representations clearly correspond to the same observation. The consistency in small-scale structure above and below the main peak is excellent. Even so, the rms difference in electron density values is $4.0 \times 10^3\ cm^{-3}$. Above and below the main peak, differences are on the order of $2 \times 10^3\ cm^{-3}$, but differences around the main peak are on the order of $1.2 \times 10^4\ cm^{-3}$. This is caused by a 3 km difference in the values of peak altitude.

Panel (d) of Figure 1 shows profiles for the ingress occultation on orbit 29. These two representations clearly correspond to the same observation. The consistency in small-scale structure above and below the main peak is excellent, but values of peak altitude differ by 4 km.

Panel (e) of Figure 1 shows profiles for the ingress occultation on orbit 31. These two representations clearly correspond to the same observation. The consistency in small-scale structure above and below the main peak is excellent, but electron density values are offset systematically by about $10^4\ cm^{-3}$.

Panel (f) of Figure 1 shows profiles for the ingress occultation on orbit 33. These two representations clearly correspond to the same observation, but offsets in altitude are apparent.

Panel (g) of Figure 1 shows profiles for the ingress occultation on orbit 34. These two representations clearly correspond to the same observation, but offsets in electron density and altitude are apparent.

Panel (h) of Figure 1 shows profiles for the ingress occultation on orbit 35. These two representations clearly correspond to the same observation, but offsets in electron density and altitude are apparent.

Panel (i) of Figure 1 shows profiles for the ingress occultation on orbit 37. These two representations clearly correspond to the same observation.

Panel (j) of Figure 1 shows profiles for the egress occultation on orbit 45. These two representations clearly correspond to the same observation, but electron density values are offset systematically by about $4 \times 10^3\ cm^{-3}$.

Panel (k) of Figure 1 shows profiles for the ingress occultation on orbit 53. These two representations clearly correspond to the same observation.

Panel (l) of Figure 1 shows profiles for the ingress occultation on orbit 55. These two representations clearly correspond to the same observation, and the agreement is excellent, with an rms difference in electron density values of $1.5 \times 10^3\ cm^{-3}$, only slightly larger than the nominal uncertainty in NSSDC electron density values of $10^3\ cm^{-3}$. Justification for this uncertainty is provided in Appendix A.

Panel (a) of Figure 2 shows the peak electron density values from these observations, and panel (b) of Figure 2 shows the differences in peak electron density values. The rms difference is $3500 cm^{-3}$. Panel (c) of Figure 2 shows the peak altitude values from these observations, and panel (d) of Figure 2 shows the differences in peak altitude values. The rms difference is 3.5 km.

These values of peak altitude and peak electron density can be compared against another source. Table 1 of Cravens et al. (1981) lists values for ingress occultations on orbits 1–40, as well as for observations in late 1979 and late 1980. When corrected for different reference radii (6052 km for Cravens et al. (1981), 6051.8 km in our preparation of the NSSDC profiles), NSSDC and Cravens peak altitudes differ by less than 0.1 km in eight of nine instances, with the difference being less than 1 km in the other instance. NSSDC and Cravens peak density values also agree well. The rms difference is less than $400\ cm^{-3}$, or less than 1%.

We conclude that the NSSDC profiles and the profiles used by Cravens et al. (1981) are practically identical. Yet it is not clear whether the NSSDC profiles and the profiles published in Kliore (1992) are identical. There are four instances in which the rms difference between the NSSDC and graphical profiles exceeds $4000 cm^{-3}$: the ingress occultations on orbit 20 ($6.5 \times 10^3 cm^{-3}$), orbit 22 ($1.2 \times 10^4 cm^{-3}$), orbit 31 ($8.7 \times 10^3 cm^{-3}$), and orbit 35 ($6.2 \times 10^3 cm^{-3}$). If the recovered graphical profiles are set aside and the NSSDC profiles shown in Figure 1 are compared directly to Figure 7(a) in Kliore (1992), then differences are

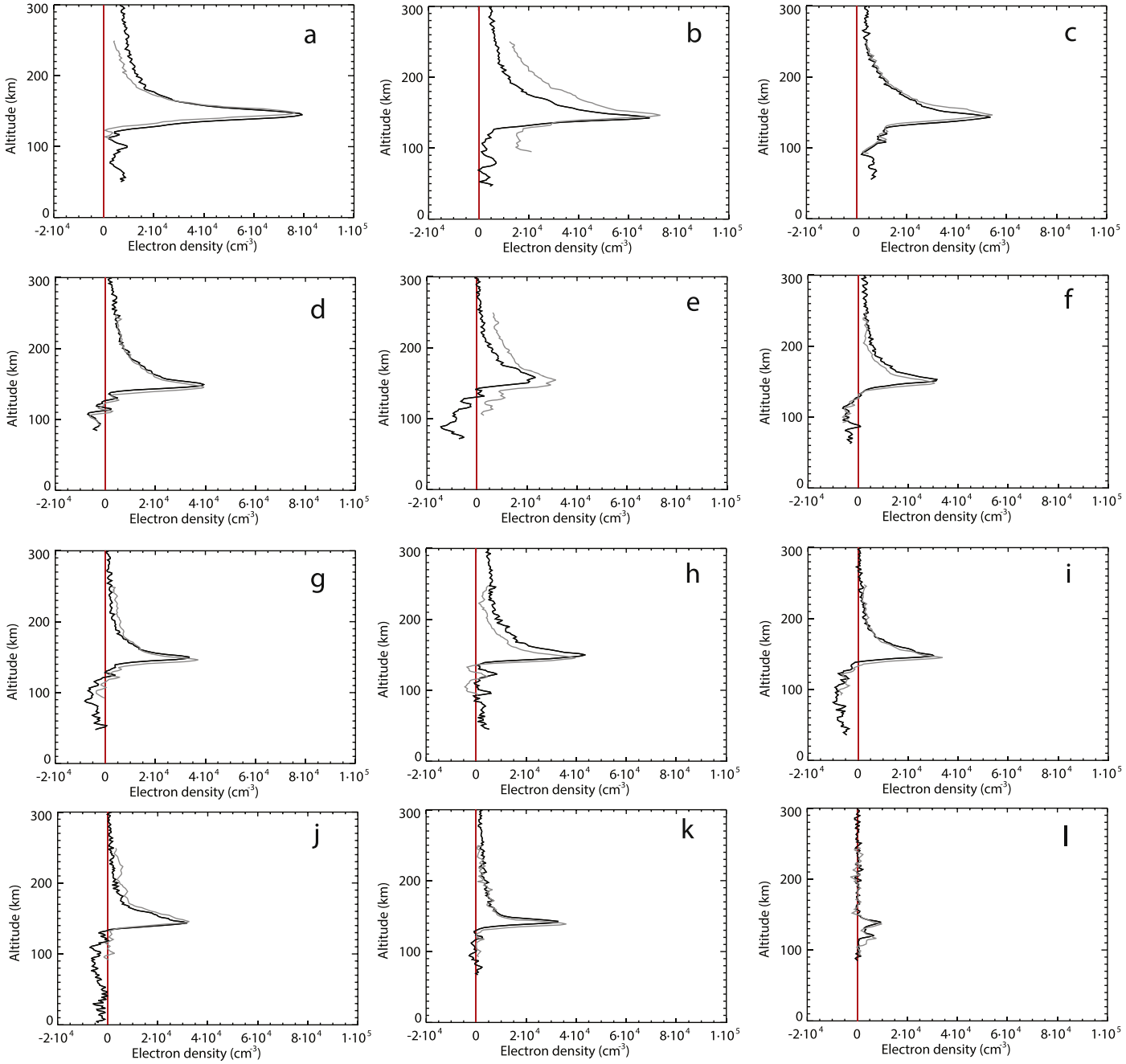

Figure 1. (a) Comparison of the NSSDC (black) and graphical (gray) representations of the ionospheric profile from the ingress occultation on orbit 20. The vertical red line indicates zero. (b) As panel (a), but for orbit 22. (c) As panel (a), but for orbit 26. (d) As panel (a), but for orbit 29. e. As panel (a), but for orbit 31. (f) As panel (a), but for orbit 33. (g) As panel (a), but for orbit 34. (h) As panel (a), but for orbit 35. (i) As panel (a), but for orbit 37. (j) As panel (a), but for the egress occultation on orbit 45. (k) As panel (a), but for orbit 53. (l) As panel (a), but for orbit 55.

apparent. Figure 7(a) in Kliore (1992) shows 11 electron density profiles from PVO orbits 20–37 in a single panel. The density axis is linear, and each successive profile is offset from its neighbor by 2×10^4 cm^{-3}. The ingress occultation on orbit 20, for which SPICE yielded a solar zenith angle of 90°.72, is the first profile in Figure 7(a) in Kliore (1992), which is labeled with a solar zenith angle of 90°.7. Electron density values near 100 km in Kliore (1992) are occasionally zero as the line indicating the electron density values intersects the relevant axis. The corresponding electron density values in the NSSDC profile (panel (a) of Figure 1) are never less than 2000 cm^{-3}, however.

The ingress occultation on orbit 22, for which SPICE yielded a solar zenith angle of 91°.51, is the second profile in Figure 7(a) in Kliore (1992), which is labeled with a solar zenith angle of 91°.4. Electron density values near 100 km in Kliore (1992) are clearly never less than 10^4 cm^{-3}. The relevant line in Figure 7(a) in Kliore (1992) is between 30 and 40 $\times 10^3$ cm^{-3}, when zero has been offset to 20 $\times 10^3$ cm^{-3}. Yet corresponding electron density values in the NSSDC profile (panel (b) of Figure 1) are less than 5×10^3 cm^{-3}.

The ingress occultation on orbit 31, for which SPICE yielded a solar zenith angle of 95°.37, is the fifth profile in Figure 7(a)

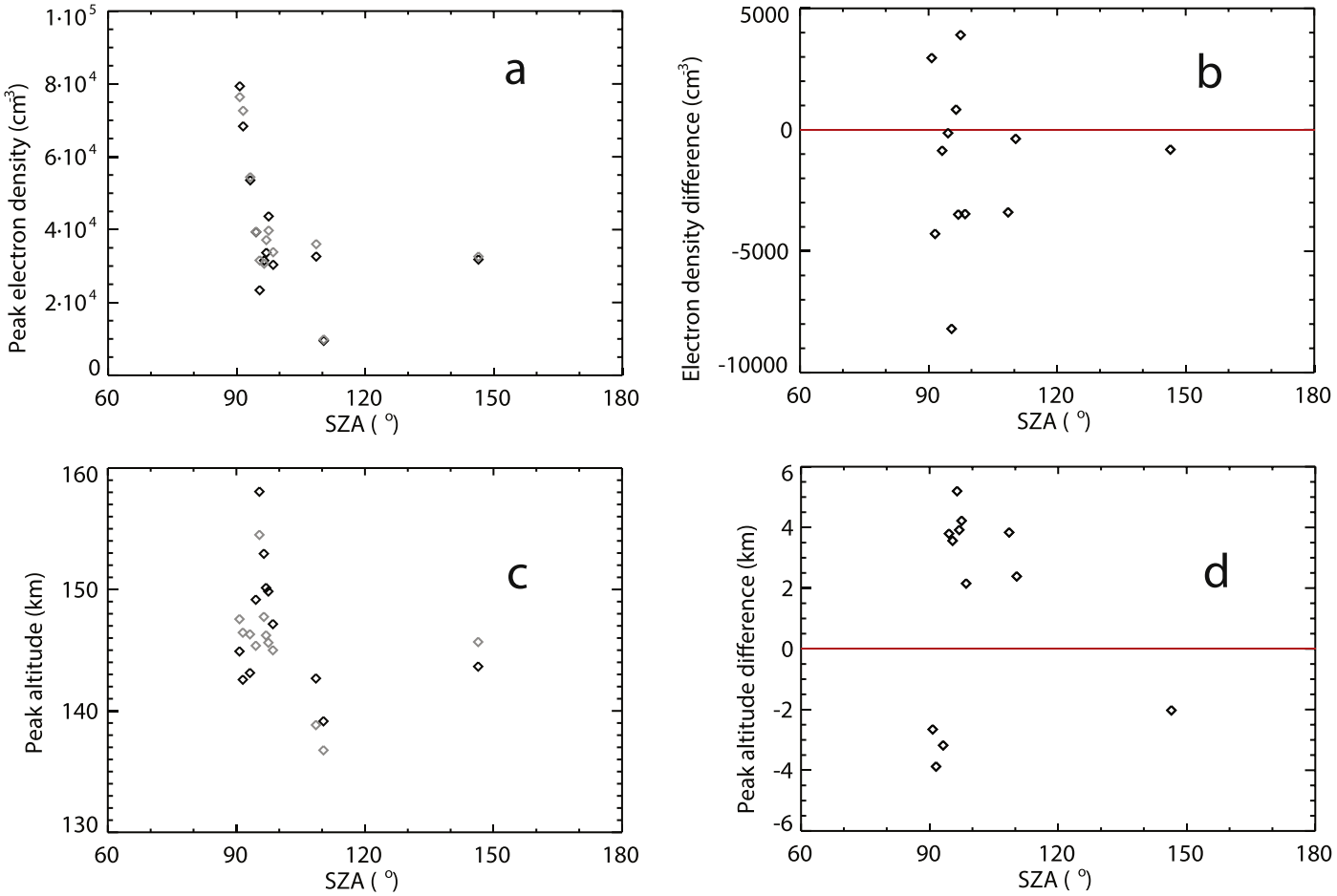

Figure 2. a. Dependence of peak electron density on solar zenith angle for observations for which both NSSDC (black) and graphical (gray) representations are available. (b) Difference between the NSSDC and graphical values of peak electron density shown in panel (a). The horizontal red line indicates zero. (c) Dependence of peak altitude on solar zenith angle for observations for which both NSSDC (black) and graphical (gray) representations are available. (d) Difference between NSSDC and graphical values of peak altitude shown in panel (c) The horizontal red line indicates zero.

in Kliore (1992), which is labeled with a solar zenith angle of 95°.3. Electron density values near 100 km in Kliore (1992) are clearly never less than zero. The relevant line in Figure 7(a) in Kliore (1992) is greater than 80 $\times 10^3$ cm^{-3}, when zero has been offset to 80 $\times 10^3$ cm^{-3}. The corresponding electron density values in the NSSDC profile (panel (e) of Figure 1) are less than -5×10^3 cm^{-3}, however.

The ingress occultation on orbit 35, for which SPICE yielded a solar zenith angle of 97°.47, is the ninth profile in Figure 7(a) in Kliore (1992), which is labeled with a solar zenith angle of 97°.4. Electron density values near 100 km in Kliore (1992) fluctuate symmetrically about zero. The relevant line on the figure fluctuates around 160 $\times 10^3$ cm^{-3}, when zero has been offset to 160 $\times 10^3$ cm^{-3}. In the recovered graphical profile (panel (h) of Figure 1), the maximum excursions are $\pm 5 \times 10^3$ cm^{-3}. Yet, the corresponding electron density values in the NSSDC profile (panel (h) of Figure 1) are less than 1×10^3 cm^{-3}.

If we set aside these four pairs and focus instead on the eight pairs of representations for which no obvious differences between the sources are apparent, then the typical rms difference in electron density values between representations is 3500 cm^{-3}. The rms difference in peak altitude values remains about 3.5 km. This suggests that the graphical recovery process may have introduced errors of 3500 cm^{-3} and 3.5 km into the recovered electron density profiles.

Another perspective on the accuracy of the graphical recovery process comes from duplicated graphical profiles. Figure 4(a) of Kliore (1992) contains the same 10 profiles as Figure 3(b) of Kliore & Luhmann (1991). The rms differences in peak electron density and peak altitude are 9×10^3 cm^{-3} and 2 km, respectively. Similarly, Figure 4(b) of Kliore (1992) contains the same 10 profiles as Figure 6(b) of Kliore & Luhmann (1991). The rms differences in peak electron density and peak altitude are 15×10^3 cm^{-3} and 1 km, respectively. It may appear disappointing that these density differences in the graphical–graphical comparison are so much greater than those found in the preceding NSSDC–graphical comparison. However, careful consideration provides reassurance.

The graphical profiles compared against the corresponding NSSDC profiles have solar zenith angles between 90° and 100°. As their peak densities were relatively small, these profiles were plotted with linear density axes in Kliore (1992). The graphical profiles compared against other graphical profiles have day-side solar zenith angles. As their peak densities were relatively large, these profiles were plotted with logarithmic density axes in Kliore & Luhmann (1991) and Kliore (1992). The rms relative differences

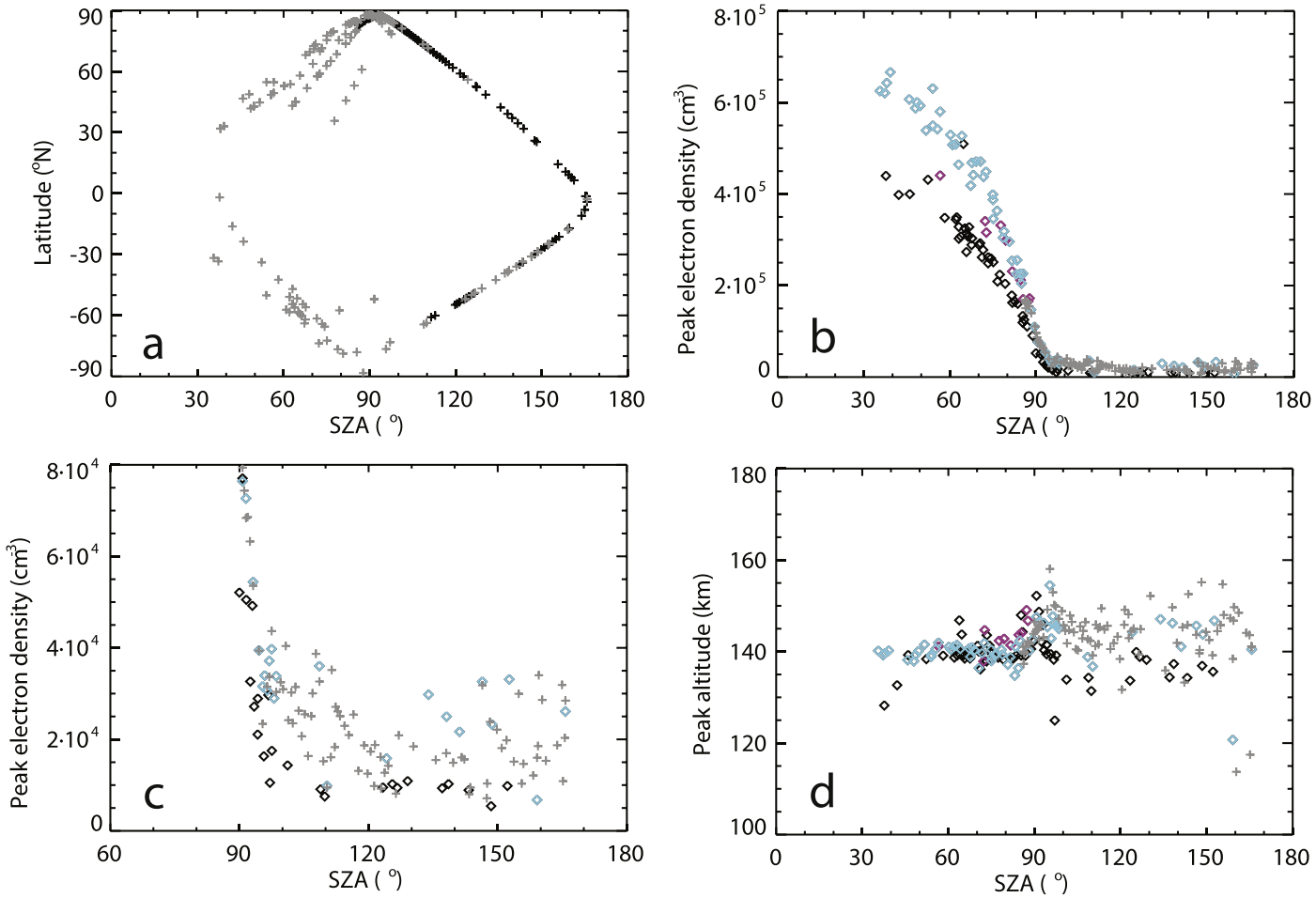

Figure 3. (a) Latitude and solar zenith angle coverage of ionospheric observations. Black symbols show NSSDC observations. Gray symbols show graphical observations. (b) Dependence of peak electron density on solar zenith angle. Gray crosses show NSSDC observations, which are all under solar maximum conditions. Diamonds show graphical observations. Cyan, magenta, and black diamonds are for observations under solar maximum, solar moderate, and solar minimum conditions, respectively. (c) As panel (b), but focused on the night-side ionosphere. (d) Dependence of peak altitude on solar zenith angle. Symbols and colors as in panel (b).

in peak density in the graphical–graphical comparisons are 3% and 6%, respectively.

As all day-side profiles in Kliore & Luhmann (1991) and Kliore (1992) were plotted with logarithmic density axes and all night-side profiles in Kliore & Luhmann (1991) and Kliore (1992) were plotted with linear density axes, we revise our previous finding. We conclude that the graphical recovery process may have introduced errors of 6% and 3.5 km into the recovered day-side density profiles and errors of 3500cm^{-3} and 3.5 km into the recovered night-side density profiles. These density errors are equal for a density of 6×10^4 cm^{-3}, which approximately equals the peak density at a solar zenith angle of 90°.

6. Overview of Electron Density Profiles

Panel (a) of Figure 3 shows the latitude and solar zenith angle coverage of the ionospheric profiles. The latitude coverage is complete from pole to pole. Solar zenith angle coverage extends from approximately 30° to 170°, leaving only small regions around the subsolar and antisolar points unsampled. However, latitude coverage and solar zenith angle coverage are correlated. A given latitude is sampled at only two solar zenith angles and vice versa.

Panel (b) of Figure 3 shows the dependence of peak electron density on solar zenith angle. As discussed in Appendix A, we set aside the values from the NSSDC profiles from the ingress occultations on orbits 38 and 72. Peak electron densities generally behave as expected. On the day side, peak densities decrease with increasing solar zenith angle and as solar conditions change from solar maximum to solar minimum. Results appear consistent with previous findings (Cravens et al. 1981; Girazian et al. 2015).

One day-side peak electron density from solar minimum conditions is unusually large. This is graphical profile k91_5b_03, the third profile in Figure 5(b) of Kliore & Luhmann (1991), which purports to contain observations from 1984. Inspection of this figure shows that electron densities are indeed unusually large at all altitudes. Possible explanations include the following: (A) the observation occurred during a brief period of elevated solar irradiance, such as a solar flare; (B) the observation, which is included in a set of observations from 1984, actually occurred in a different year that was closer to solar maximum; and (C) densities in this profile were accidentally multiplied by a factor of 1.5 prior to the production of this figure. It is exceedingly unlikely that a radio occultation of a few minutes duration happened to occur during a solar flare at solar minimum conditions. Although we cannot definitively resolve this issue, we judge it most likely that this profile comes from a time of solar maximum conditions, not 1984.

Panel (c) of Figure 3 highlights the behavior of peak electron density values on the night side. In the near-terminator region, peak electron density values at solar maximum decrease steadily from $\sim 6 \times 10^4\,\mathrm{cm}^{-3}$ at 90° solar zenith angle to $(1–2) \times 10^4\,\mathrm{cm}^{-3}$ at 120°. In the same region, peak electron density values at solar minimum decrease steadily from $\sim 5 \times 10^4\,\mathrm{cm}^{-3}$ at 90° to $1 \times 10^4\,\mathrm{cm}^{-3}$ at 110°. Beyond 120°, peak electron density values are $1–3 \times 10^4\,\mathrm{cm}^{-3}$ at solar maximum and $\sim 1 \times 10^4\,\mathrm{cm}^{-3}$ at solar minimum. Consequently, peak electron density values at solar maximum are smallest at 120° and larger both closer to the terminator and closer to the antisolar point. Yet, peak electron density values at solar minimum are uniformly small at 110° and above. This likely reflects the increased strength of an ion production mechanism at solar maximum, such as enhanced particle precipitation. Results appear consistent with previous findings (Zhang et al. 1990).

Panel (d) of Figure 3 shows the dependence of peak altitude on solar zenith angle. As discussed in Appendix A, we set aside the values from the NSSDC profiles from the ingress occultations on orbits 38 and 72. On the day side, peak altitude is uniform at 140 km. These peak altitudes from PVO are slightly lower than the 141 ± 1 km value found by Girazian et al. (2015) in Venus Express radio occultation profiles. Neither the PVO nor the Venus Express data set suggest that day-side peak altitude varies with solar activity. Brace & Kliore (1991) stated that peak altitude in unpublished PVO observations from 1984–1987 (solar minimum) were 5 km lower than peak altitudes at solar maximum. No such change in peak altitude is apparent in the PVO profiles from 1984 to 1987 that we recovered from Kliore & Luhmann (1991) and Kliore (1992). Perhaps the discussion in Brace & Kliore (1991) was based upon preliminary versions of electron density profiles, but Kliore & Luhmann (1991) and Kliore (1992) used reprocessed versions of these electron density profiles. The peak altitude increases with increasing solar zenith angle as the terminator is approached. On the night side, the peak altitude is 5–10 km higher at solar maximum than solar minimum. Results appear consistent with previous findings (Cravens et al. 1981; Brace et al. 1983; Zhang et al. 1990; Kliore et al. 1991).

We identified five data points in panel (d) of Figure 3 as potential outliers—the NSSDC profile from the egress occultation on orbit 72 and graphical profiles k91_5a_01, k91_5b_01, k92_7b_10, and k92_8a_10. Here, we assess those five potential outliers.

The NSSDC profile from the egress occultation on orbit 72 has a solar zenith angle of 165° and a peak altitude of 117 km. This is a double-layered profile, a morphology that is common on the deep night side (Brace et al. 1983; Pätzold et al. 2007). The upper layer is near 150 km, the typical peak altitude for the deep night-side ionosphere under solar maximum conditions. This lower layer occurs at the usual altitude for lower layers in double-layered profiles. In this observation, electron densities are greater in the lower layer than in the upper layer, which is relatively unusual. The NSSDC profile from the egress occultation on orbit 80 is similar. However, the low-altitude portion of this profile, which includes the identified peak, is questionable. This is described more fully in Appendix A. We consider that the observed double-layered morphology is robust but reserve judgment on whether the lower layer or the upper layer should have the largest electron density.

The graphical profile k91_5a_01, the first profile in Figure 5(a) of Kliore & Luhmann (1991), is from 1984. It has a solar zenith angle of 37°.68 and a peak altitude of 128 km, about 10 km lower than unusual. This is not the result of an egregious error in the graphical recovery process. The peak altitude is clearly relatively low in the published figure itself. It is unlikely that this low peak altitude resulted from the poor orbit determination discussed below, which was limited to the early period of the mission when periapsis was at thermospheric altitudes.

The graphical profile k91_5b_01, the first profile in Figure 5(b) of Kliore & Luhmann (1991), is from 1984. Similarly, it has a solar zenith angle of 42°.15 and a peak altitude of 133 km. Again, the peak altitude is clearly relatively low in the published figure itself.

The graphical profile k92_7b_10, the 10th profile in Figure 7(b) of Kliore (1992), is from 1986. It has a solar zenith angle of 97°.08 and a peak altitude of 125 km, about 15 km lower than unusual. Inspection of the published figure shows that the main ionospheric layer is relatively broad in this observation. Moreover, a single electron density value near the bottom of this layer is slightly enhanced, forming a small, narrow spike that is the largest electron density value in the profile.

The graphical profile k92_8a_10, the 10th profile in Figure 8(a) of Kliore (1992), is from 1979. It has a solar zenith angle of 159°.14 and a peak altitude of 121 km. This profile was acquired on the deep night side under solar maximum conditions. Several such profiles have two layers, an upper one around 150 km and a lower one around 120 km. Usually, electron densities are greater in the upper layer than in the lower layer. In this observation, no upper layer is apparent and densities in the lower layer are not much larger than the magnitude of density fluctuations throughout the profile, which is an indication of the density uncertainty.

Cravens et al. (1981) raised concerns about the accuracy of orbit determination and resultant radial distances for the ingress occultations on orbits 1, 9, 10, 14, 19, 24, 325, and 332. Of these, NSSDC profiles are available for orbits 1, 10, 19, and 24. Their peak altitudes appear normal.

Figure 4 shows selected profiles at solar zenith angles near 40°, 50°, 60°, 70°, 80°, and 90°. All of these observations are from solar maximum conditions. Panel (a) of Figure 4 uses a linear scale for electron density, whereas panel (b) of Figure 4 uses a logarithmic scale for electron density. Different features are highlighted by the different scales: a linear scale highlights the main peak, a logarithmic scale highlights the top side. Panel (a) of Figure 4 shows the peak density decreasing with increasing solar zenith angle, while the peak altitude does not change. Panel (b) of Figure 4 shows the considerable extent of the top-side ionosphere and illustrates that this region is less controlled by solar zenith angle than the main peak.

Figure 5 shows selected profiles at solar zenith angles near 50° and 70° from solar minimum and solar maximum conditions. It illustrates that peak density decreases as solar activity decreases. For example, the peak density in the profile at 50° from solar minimum is the same as in the profile at 70° from solar maximum. Yet, peak altitude is insensitive to solar activity. Top-side electron densities on the day side are markedly greater at solar maximum than at solar minimum.

Panel (a) of Figure 6 shows selected profiles at solar zenith angles near 120° from solar minimum and solar maximum conditions. An upper layer is present around 140 km in both profiles, and a lower layer is present around 120 km in one of the profiles. These two morphologies (a single layer at 140 km, two

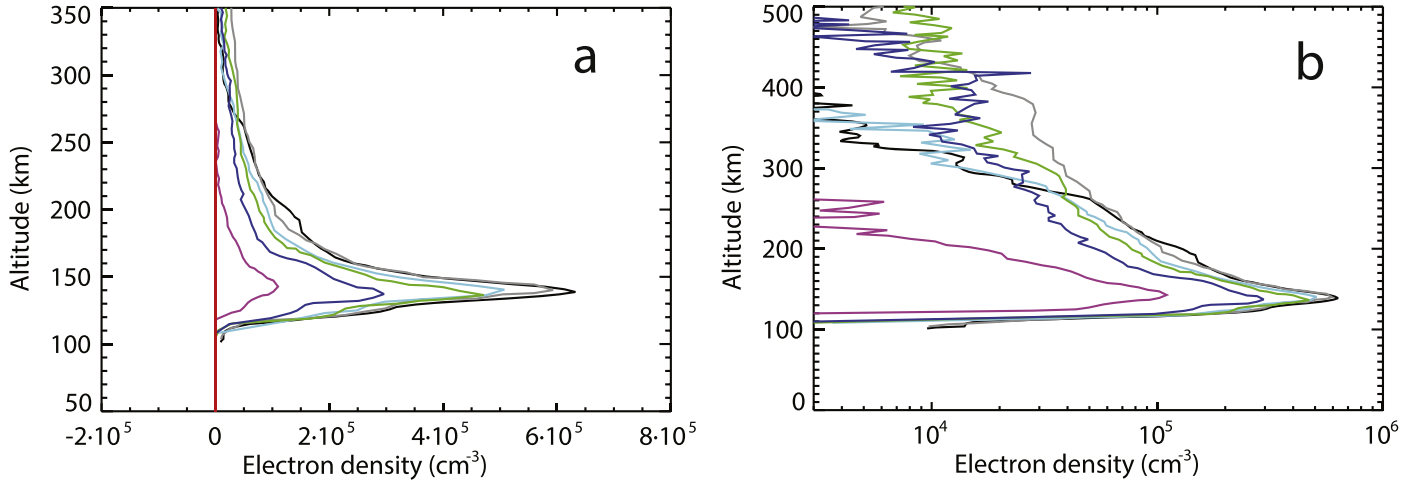

Figure 4. (a) Six selected graphical electron density profiles at solar zenith angles of 40° (k92_4a_01, black), 50° (k91_3b_02, gray), 60° (k91_4a_04, cyan), 70° (k91_4a_06, green), 80° (k91_4a_08, blue), and 90° (k91_4a_1, magenta). The vertical red line highlights zero. (b) As panel (a), but with a logarithmic axis.

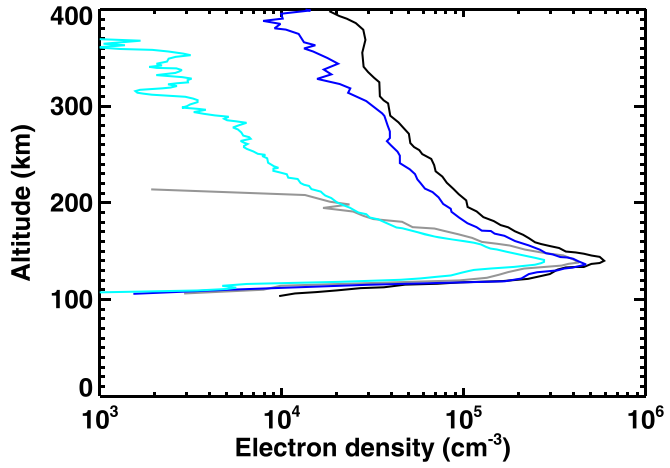

Figure 5. Four selected graphical electron density profiles. The black profile (k91_3b_02) was acquired at 50° solar zenith angle under solar maximum conditions. The blue profile (k91_4a_06) was acquired at 70° solar zenith angle under solar maximum conditions. The gray profile (k91_5a_03) was acquired at 50° solar zenith angle under solar minimum conditions. The cyan profile (k92_4b_05) was acquired at 70° solar zenith angle under solar minimum conditions.

layers at 120 km and 140 km) are common in the night-side ionosphere (e.g., Brace et al. 1983). Peak density is around 10^4 cm^{-3} in both profiles. Although significantly smaller than the day-side peak density, this value is significantly greater than would be expected for photochemical equilibrium of photoproduced molecular ions at a slowly rotating planet (Schunk & Nagy 2009). Panel (b) of Figure 6 shows selected profiles at solar zenith angles near 150° from solar minimum and solar maximum conditions. An upper layer is present around 140 km in both profiles. Peak density is around 3×10^4 cm^{-3} in the solar maximum profile, but is only 10^4 cm^{-3} in the solar minimum profile. These two panels illustrate how the night-side ionosphere changes from solar minimum to solar maximum. At solar minimum, the night-side peak density is 10^4 cm^{-3} at all solar zenith angles, whereas at solar maximum, the night-side peak density is 10^4 cm^{-3} at 120°, but greater at both smaller and larger solar zenith angles.

Panel (c) of Figure 6 shows other examples of night-side double layers. These examples illustrate the stability of the altitudes of both layers and that electron density values are usually greater in the upper layer.

Panel (d) of Figure 6 shows examples of a shoulder in the top-side ionosphere around 250 km. This feature was noted in reports of the Mariner 10 day-side occultation (Fjeldbo et al. 1975) and early PVO radio occultation observations (Kliore et al. 1979b). Several hypotheses for its origin have been set forth, including chemical effects associated with O^+ ions (Fox & Sung 2001) and magnetohydrodynamic effects (Shinagawa et al. 1991). An analogous feature has also been reported at Mars (Mayyasi et al. 2018).

7. Summary

We have recovered, validated, and archived an extensive set of ionospheric electron density profiles from radio occultations by PVO. Some ionospheric electron density profiles were recovered from figures in publications by the PVO experimenters, and some were recovered from files maintained by the NSSDC.

We have recovered 94 sets of NSSDC electron density data products, of which 93 were suitable for archiving. The characteristic value of the scatter in NSSDC electron density measurements above ionospheric altitudes is 1000cm^{-3}, which can be adopted as an estimate of the uncertainty in NSSDC electron density measurements. The vertical resolution of the NSSDC electron density profiles is typically 1–2 km. Overall, the quality of the NSSDC ionospheric electron density profiles is good at and above the main ionospheric peak. As described more fully in Appendix A, systematic biases are common, but not ubiquitous, at lower altitudes. Data users intending to investigate the lower regions of the ionosphere are advised to thoughtfully assess each individual profile.

We have recovered 154 sets of graphical electron density data products, all of which were suitable for archiving. The archived set of graphical electron density data products includes two representations (observation present in multiple sources) of the results from 20 observations. There are 12 electron density data products for which both NSSDC and graphical representations exist. Based on comparisons between these pairs of electron density data products, we find that the graphical recovery process may have introduced errors of 6%

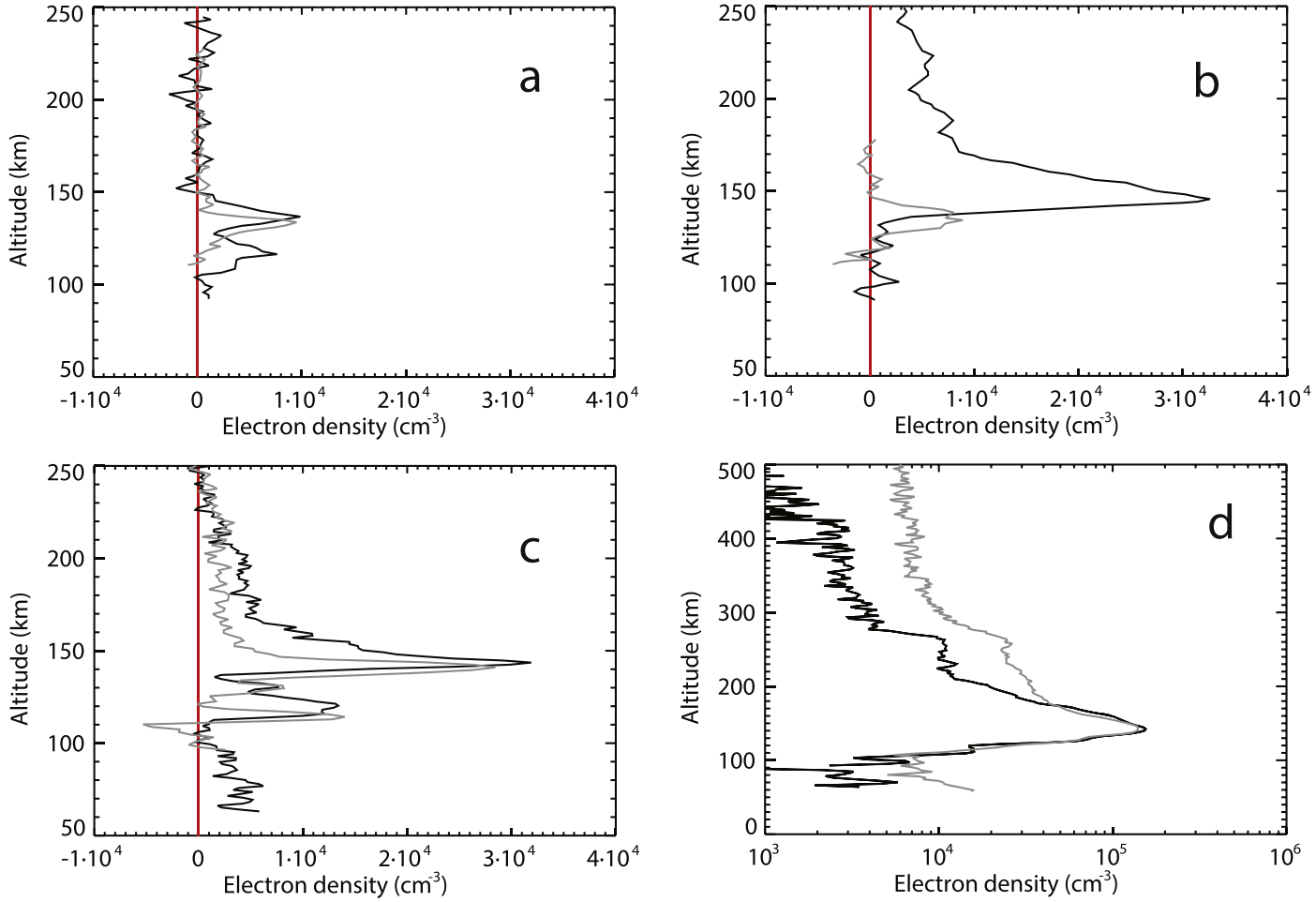

Figure 6. (a) Two selected graphical electron density profiles. The black profile (k92_8a_02) was acquired at 110° solar zenith angle under solar maximum conditions. The gray profile (k92_8b_02) was acquired at 120° solar zenith angle under solar minimum conditions. The vertical red line highlights zero. (b) Two selected graphical electron density profiles. The black profile (k92_8a_07) was acquired at 150° solar zenith angle under solar maximum conditions. The gray profile (k92_8b_09) was acquired at 150° solar zenith angle under solar minimum conditions. The vertical red line highlights zero. (c) Two selected NSSDC electron density profiles with solar zenith angle around 165°. The black profile shows the egress occultation on orbit 66. The gray profile shows the egress occultation on orbit 69. The vertical red line highlights zero. (d) Two selected NSSDC electron density profiles with solar zenith angle around 88°. The black profile shows the ingress occultation on orbit 10. The gray profile shows the ingress occultation on orbit 13.

and 3.5 km into the recovered day-side electron density profiles and errors of 3500 cm^{-3} and 3.5 km into the recovered night-side electron density profiles. These density errors are equal for a density of 6×10^4 cm^{-3}, which approximately equals the peak density at a solar zenith angle of 90°.

More than 200 distinct electron density profiles have been recovered. This is an order of magnitude more than the number of accessible electron density profiles from Venera 15/16. It is comparable to the number of electron density profiles acquired by Venus Express, which can be requested from the experimenters.

Overall, the electron density data products show the expected trends with altitude, solar zenith angle, and solar activity. The recovered profiles and comprehensive documentation are available at https://hdl.handle.net/2144/41269. In August 2020, this material was delivered to the PDS for review and archiving. These data products are ready for use in scientific investigations of the ionosphere of Venus and related topics. For instance, the electron density profiles could be synthesized with in situ compositional information to develop a more comprehensive understanding of the vertical structure of the ionosphere.

This work was supported, in part, by NASA award NNX17AK95G. We thank Robert Putnam and the Boston University Research Computing Services for extraction of data from the NSSDC package and Casey Flynn for support of the recovery of graphical profiles. We thank two anonymous reviewers.

Appendix A
Overview

The structure of this appendix is as follows. Appendix B presents the spatial and temporal extent of PVO radio occultation observations. Appendix C assesses the quality of the ionospheric profiles recovered from files maintained by the National Space Science Data Center (NSSDC). Appendix D describes the ionospheric profiles recovered from figures in published articles and outlines the process by which ancillary information was obtained for these ionospheric profiles.

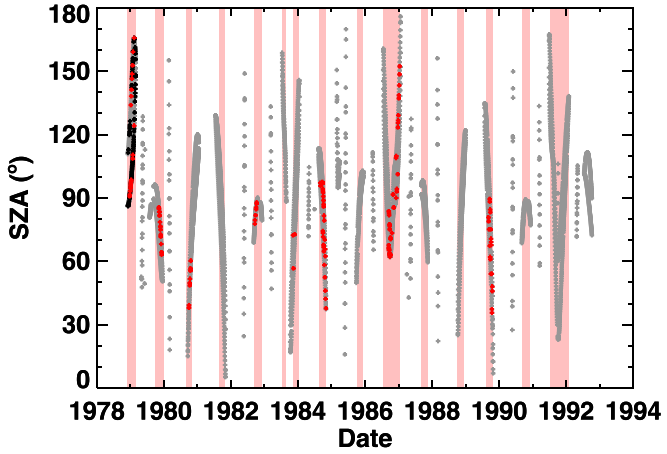

Figure 7. Solar zenith angle coverage of PVO occultation opportunities. Gray symbols show all occultation opportunities during the mission. Black symbols show occultations for which NSSDC ionospheric profiles exist. Red symbols show occultations for which graphical ionospheric profiles were recovered. Pink regions show the occultation seasons listed in Table 2.

Appendix B
Spatial and Temporal Extent of PVO Radio Occultation Observations

The SPICE kernels online at http://naif.jpl.nasa.gov/pub/naif/PIONEER12/kernels/spk/ do not cover the full duration of the PVO mission. However, ASCII tables of the PVO position in a standard reference frame are available at 12 second resolution from https://pds-ppi.igpp.ucla.edu/data/PVO-V-POS-5–VSOCOORDS-12SEC-V1.0/. Standard SPICE tools were used to generate a low-fidelity trajectory kernel for PVO from these tables. We then used this trajectory kernel to find the times and locations of each occultation point over the complete duration of the PVO mission. The occultation point was defined as the time and location where the ray path of the radio signal transmitted from the spacecraft to Earth has a closest approach distance to Venus equal to the representative ionospheric radial distance of 6200 km. Specifically, we found the date and time (OCC_TIME_SPICE), solar zenith angle (SZA_SPICE), areocentric latitude (LAT_SPICE), areocentric east longitude (LON_SPICE), and local solar time (LST_SPICE).

The periods when occultation opportunities occurred are shown in Figure 7. Periods when radio occultation observations were acquired tended to cluster into "occultation seasons." The dates of these occultation seasons can be determined from inspection of the temporal coverage of the raw radio occultation data archived at https://pds-ppi.igpp.ucla.edu/archive1/PV04_0001/ to PV04_0066/. However, this source provides confusing information for occultation seasons 1–4. For these seasons, we adopt the dates stated in Figure 1 of Cravens et al. (1981), supported by Table 1 of Kliore (1985). Note that Table 1 of Kliore (1985) contains a typographical error for season 4 (IV) in which the year is incorrectly specified as 1980. The correct year is 1981. Table 2 provides the dates of the 15 occultation seasons observed by PVO.

Appendix C
NSSDC Ionospheric Profiles

The quality of some NSSDC ionospheric profiles is questionable.

Table 2
Occultation Seasons

Season	Start	End
1	1978 Dec	1979 Feb
2	1979 Oct	1979 Dec
3	1980 Sep	1980 Oct
4	1981 Sep	1981 Oct
5	1982 Sep 10	1982 Dec 5
6	1983 Jul 17	1983 Aug 22
7	1983 Nov 7	1984 Jan 11
8	1984 Aug 18	1984 Nov 1
9	1985 Oct 5	1985 Dec 1
10	1986 Jul 20	1987 Jan 18
11	1987 Sep 10	1987 Nov 16
12	1988 Oct 8	1988 Dec 13
13	1989 Aug 17	1989 Oct 26
14	1990 Sep 7	1990 Dec 1
15	1991 Jul 8	1992 Jan 28

In profile pvoro_nssdc_eden_0038_n_cl_d_v01_r00.tab (panel (a) of Figure 8), the ionospheric peak is at a radial distance of 6234 km (equivalent to an altitude of 182 km), which is unusually high for its solar zenith angle of 99°. Upon inspection, this profile appears to be generally similar to other profiles, except that it is displaced upwards by about 30–40 km. Furthermore, electron density values below 6200 km are systematically negative by $\sim 5 \times 10^3\ \mathrm{cm}^{-3}$, rather than scattered around zero as expected. Cravens et al. (1981) also raised concerns about this observation, noting an unusually large uncertainty in ionospheric peak altitude. They attributed this to "large errors in orbit determination because of uncertainties in atmospheric drag near periapsis." The simplest explanation for the unrealistically high peak altitude is that the assignment of radial distances to time-referenced data samples was systematically biased. As an ad hoc solution, we advise that data points below 6200 km be set aside by data users, then remaining points be shifted downwards by ~35 km. More cautious data users may wish to discard the whole profile.

In profile pvoro_nssdc_eden_0040_n_cl_d_v01_r00.tab (panel (b) of Figure 8), the lowest altitude electron density value, which exceeds $6 \times 10^4\ \mathrm{cm}^{-3}$, is clearly erroneous. We advise that this data point be set aside by data users.

In profile pvoro_nssdc_eden_0046_n_cl_d_v01_r00.tab (panel (c) of Figure 8), data gaps exist. There is a 10 km gap around a radial distance of 6285 km and a pair of 7 km gaps around a radial distance of 6400 km. The vertical resolution in the rest of this profile is about 1.5 km. Although this issue does not invalidate this profile, we advise that data users inspect it closely before using it.

In profile pvoro_nssdc_eden_0050_n_cl_d_v01_r00.tab (panel (d) of Figure 8), electron densities are clearly erroneous at radial distances less than 6090 km, with some values exceeding $5 \times 10^4\ \mathrm{cm}^{-3}$. We advise that these data points be set aside by data users.

In profile pvoro_nssdc_eden_0058_x_cl_d_v01_r00.tab (panel (e) of Figure 8), a layer with electron density values of $2–3 \times 10^4\ \mathrm{cm}^{-3}$ is present at a radial distance of 6110–6120 km, or 60–70 km altitude. The differential Doppler measurement technique is questionable at such low altitudes as *S*-band and *X*-band signals begin to follow different paths (Pätzold et al. 2004, 2009; Withers et al. 2012). We advise that data points at radial distances below 6150 km be set aside by data users.

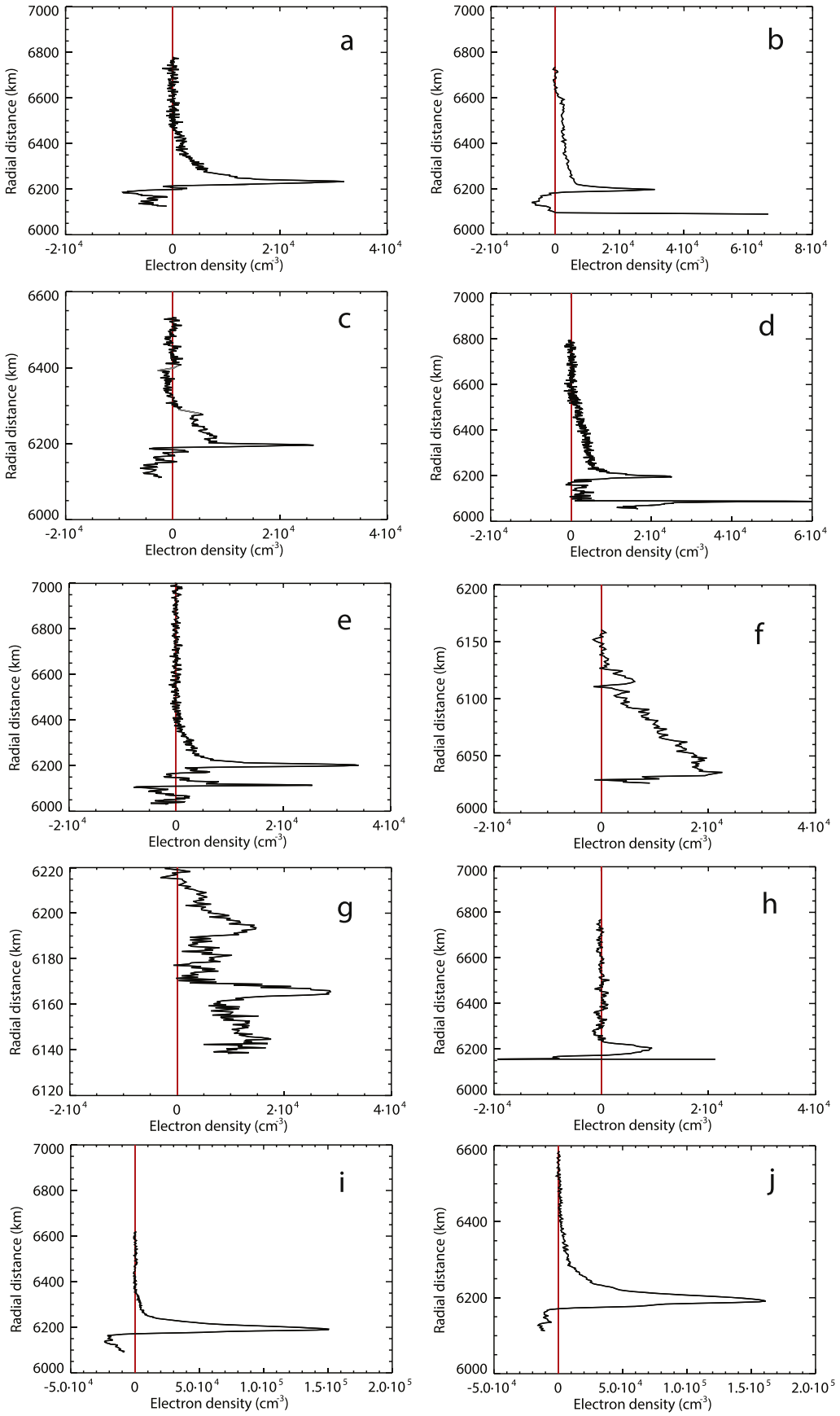

Figure 8. (a) The NSSDC ionospheric profile from the ingress occultation on orbit 38. The vertical red line indicates zero. (b) As panel (a), but for orbit 40. (c) As panel (a), but for orbit 46. (d) As panel (a), but for orbit 50. (e) As panel (a), but for the egress occultation on orbit 58. (f) As panel (a), but for orbit 72. (g) As panel (a), but for the egress occultation on orbit 80. (h). As panel (a), but for orbit 82. (i) As panel (a), but for orbit 1. (j) As panel (a), but for orbit 5.

In profile pvoro_nssdc_eden_0072_n_cl_d_v01_r00.tab (panel (f) of Figure 8), radial distances range from 6030 km to 6160 km, or –20 km to 110 km altitude. Furthermore, electron density values systematically increase from 0 at 6110 km to 2×10^4 cm^{-3} at 6030 km. We advise that this profile be set aside by data users.

In profile pvoro_nssdc_eden_0080_x_cl_d_v01_r00.tab (panel (g) of Figure 8), electron density values at 6140–6160 km, which are usually near zero, are around 1×10^4 cm^{-3}. Also, a layer with electron density values of 2–3 $\times 10^4$ cm^{-3} is present at a radial distance of 6160–6170 km, or 110–120 km altitude. Such layers are fairly common on the night side (e.g., Brace et al. 1983), but the electron density gradient on the top side of this layer is unusually steep. The rest of the profile appears normal. We advise that data points at radial distances below 6170 km be treated with caution by data users.

In profile pvoro_nssdc_eden_0082_n_cl_d_v01_r00.tab (panel (h) of Figure 8), the two lowest altitude electron density values, which are -2×10^4 cm^{-3} and 2×10^4 cm^{-3}, are clearly erroneous. We advise that these data points be set aside by data users. Furthermore, the main ionospheric layer in this profile is unusually broad with an FWHM of 37 km and the smooth sweep of the bottom side of the layer to negative electron density values casts doubt on the validity of the observed layer itself. We advise that data users inspect this profile carefully before using it.

Negative values of electron density, although unphysical, are not intrinsically concerning. Instead, values of electron density that are normally distributed around zero indicate the uncertainty in measured values of electron density. However, sets of values of electron density that are systematically less than zero are concerning, as they indicate the presence of systematic bias in measured values of electron density. Such behavior is common below 6200 km, as previously seen in panels (a), (c), and (h) of Figure 8.

It is also common in profiles that are otherwise robust, as shown in panels (i) and (j) of Figure 8. Instances of electron density values less than -5×10^3 cm^{-3} are particularly concerning. We advise that data users interested in behavior below the main peak of the ionosphere inspect each profile they plan to use and consider whether systematic biases are apparent in the low-altitude electron density values. Systematic biases may render a profile of little value to the intended scientific investigation.

Uncertainties in the electron density values reported for a given ionospheric profile can be estimated as the rms of electron density values at high altitudes, where the altitude range is selected to be above the regions where appreciable electron densities are present. Figure 9 shows how this rms value depends on the radial distance of the uppermost data point in each profile. When the uppermost data point in an electron density profile occurs at a relatively low radial distance, the set of "high-altitude" electron density values includes measurements that sample the ionosphere. Hence, rms values for these profiles are artificially large. We suggest that 1000 cm^{-3} is a reasonable representative value for the uncertainty in these electron density profiles. Data users can either adopt this as a default value or implement methods for assigning a specific uncertainty value to each electron density profile.

We have prepared 93 NSSDC ionospheric electron density profiles for archiving. We advise data users to set aside profile pvoro_nssdc_eden_0072_n_cl_d_v01_r00.tab and to consider setting aside profile pvoro_nssdc_eden_0038_n_cl_d_v01_r00.tab. This leaves either 91 or 92 NSSDC ionospheric electron density profiles deemed useful for scientific investigations. Overall, the quality of the NSSDC ionospheric electron density profiles is good at and above the main ionospheric peak. Systematic biases are common, but not ubiquitous, at lower altitudes. We advise data users intending to investigate the lower regions of the ionosphere to thoughtfully assess each individual profile.

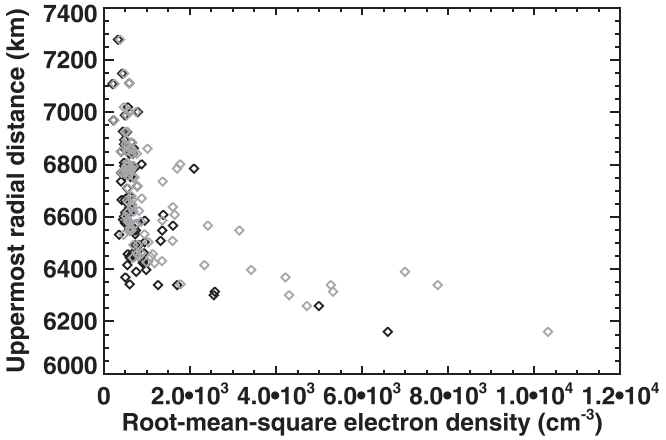

Figure 9. Dependence of the rms of electron density values in the top-side ionosphere on the uppermost radial distance. Black symbols are for a "top side" that is the uppermost 100 km of the observed profile. Gray symbols are for a "top side" that is the uppermost 200 km of the observed profile.

Appendix D
Graphical Electron Density Profiles

Figures in Kliore & Luhmann (1991) contain 90 profiles. Altitude range is 100 to 1000 km. All profiles are at day-side solar zenith angles and are plotted with a logarithmic density axis. Figures in Kliore (1992) contain 64 profiles. Altitude range is 0–400 km. All profiles at day-side solar zenith angles are plotted with a logarithmic density axis. All profiles at night-side solar zenith angles are plotted with a linear density axis. Figure 4(a) of Kliore (1992) contains the same 10 profiles as Figure 3(b) of Kliore & Luhmann (1991). Figure 4(b) of Kliore (1992) contains the same 10 profiles as Figure 6(b) of Kliore & Luhmann (1991). There are 154 representations of 134 profiles. Each representation is labeled by a solar zenith angle.

PDF copies of Kliore & Luhmann (1991) and Kliore (1992) were obtained. Digital files of selected figures were extracted from these articles. For each profile in each of the selected figures, a set of numerical values of altitude and electron density was recovered using the "DataThief" tool (https://datathief.org/).

Adjacent profiles often overlapped, which occasionally made it challenging to assign a data point to a specific profile. This was particularly concerning at low altitudes where electron densities change rapidly with altitude. This work was conducted using generic PDF copies provided at the publisher's website. Toward the end of this project, it was realized that the figures in the library's bound versions of the original journal issues displayed finer details than in these generic PDF copies. Colleagues considering reproducing this work are advised to start from bound versions of the original journal

issues themselves, rather than using the generic PDF copies available at the publisher's website.

Each profile is labeled by year (or pair of years) and solar zenith angle (SZA_ORIG). It is necessary to generate additional ancillary information to support the analysis and interpretation of these ionospheric observations, including the time of the observation, Venus-centric latitude, Venus-centric east longitude, local solar time, and whether the observation was ingress or egress. We generated this information using SPICE.

We matched each recovered profile to an occultation opportunity identified by SPICE as outlined below. Some matches are identified confidently, some are not. This process is described more fully in the documentation available at https://hdl.handle.net/2144/41269. Extensive detail is provided so that data users can critically evaluate the decisions made to match each recovered profile to an occultation opportunity. If data users feel an alternative match is preferable for any profile, then the accompanying tables provide the dates and times of all viable alternatives. Given a date and time, the occultation location and any other desired supporting information can be obtained using SPICE.

It should be noted that the orbital period of PVO was 24 hr, and hence successive occultation opportunities occurred at intervals of approximately 24 hr. It should also be noted that the archived raw radio occultation data (https://pds-ppi.igpp.ucla.edu/archive1/PV04_0001/ to PV04_0066/) tend to emphasize "pass number" in preference to "orbit number." Pass number presumably refers to the cumulative number of DSN tracking passes committed to PVO. Pass number is greater than orbit number by approximately 200, but this offset is not constant over the full duration of the mission. PVO in situ data are labeled by orbit number, not pass number.

Profiles plotted in Kliore (1992) are accompanied by the corresponding solar wind pressure. In principle, this information could be used to place constraints on the date when a profile was acquired. However, that information was not used in this work.

Table 1 of Cravens et al. (1981) lists many electron density profiles measured in 1978–1980. A similar table that spans 1979 to 1986 is provided in Kliore & Mullen (1989). As described more fully in the documentation available at https://hdl.handle.net/2144/41269, these lists are useful for deciding which possible occultation opportunities are most likely for a given profile.

No concerns about the quality of the graphical ionospheric profiles were noted.

ORCID iDs

Paul Withers https://orcid.org/0000-0003-3084-4581
Kerry Hensley https://orcid.org/0000-0003-4790-2928
Marissa F. Vogt https://orcid.org/0000-0003-4885-8615

References

Bauer, S. J., Brace, L. M., Taylor, H. A., Jr., Breus, T. K., & Kliore, A. J. 1985, AdSpR, 5, 233
Berman, A. L., & Ramos, R. 1980, ITGRS, 18, 11
Bougher, S. W., Hunten, D. M., & Phillips, R. J. 1997, Venus II (Tucson, AZ: Univ. Arizona Press)
Brace, L. H., Grebowsky, J. M., & Kliore, A. J. 1997, AdSpR, 19, 1203
Brace, L. H., & Kliore, A. J. 1991, SSRv, 55, 81
Brace, L. H., Taylor, H. A., Gombosi, T. I., et al. 1983, in Venus, ed. D. M. Hunten et al. (Tucson, AZ: Univ. Arizona Press), 779
Colin, L. 1977, SSRv, 20, 249
Cravens, T. E., Kozyra, J. U., Nagy, A. F., & Kliore, A. J. 1981, JGR, 86, 11323
Dalba, P. A., & Withers, P. 2019, JGRA, 124, 643
Fjeldbo, G., Seidel, B., Sweetnam, D., & Howard, T. 1975, JAtS, 32, 1232
Fox, J. L., & Kliore, A. J. 1997, in Venus II : Geology, Geophysics, Atmosphere, and Solar Wind Environment, ed. S. W. Bougher, D. M. Hunten, & R. J. Phillips (Tucson, AZ: Univ. Arizona Press), 161
Fox, J. L., & Sung, K. Y. 2001, JGR, 106, 21305
Girazian, Z., Withers, P., Häusler, B., et al. 2015, P&SS, 117, 146
Häusler, B., Pätzold, M., Tyler, G. L., et al. 2006, P&SS, 54, 1315
Hunten, D. M., Colin, L., Donahue, T. M., & Moroz, V. I. 1983, Venus (Tucson, AZ: Univ. Arizona Press)
Imamura, T., Ando, H., Tellmann, S., et al. 2017, EP&S, 69, 137
Jenkins, J. M. 1998, Final Technical Report of Grant NAGW-4450, http://hdl.handle.net/2060/19980210762
Jenkins, J. M., Steffes, P. G., Hinson, D. P., Twicken, J. D., & Tyler, G. L. 1994, Icar, 110, 79
Kliore, A. J. 1985, AdSpR, 5, 41
Kliore, A. J. 1992, in Venus and Mars: Atmospheres, ionospheres, and solar wind interactions; Proc. of the Chapman Conf., ed. J. G. Luhmann, M. Tatrallyay, & R. O. Pepin (Washington, DC: AGU), 265
Kliore, A. J., & Luhmann, J. G. 1991, JGR, 96, 21281
Kliore, A. J., Luhmann, J. G., & Zhang, M. H. G. 1991, JGR, 96, 11065
Kliore, A. J., & Mullen, L. F. 1989, JGR, 94, 13339
Kliore, A. J., & Mullen, L. F. 1990, AdSpR, 10, 15
Kliore, A. J., & Patel, I. R. 1980, JGR, 85, 7957
Kliore, A. J., & Patel, I. R. 1982, Icar, 52, 320
Kliore, A. J., Patel, I. R., Nagy, A. F., Cravens, T. E., & Gombosi, T. I. 1979a, Sci, 205, 99
Kliore, A. J., Woo, R., Armstrong, J. W., Patel, I. R., & Croft, T. A. 1979b, Sci, 203, 765
Mayyasi, M., Withers, P., & Fallows, K. 2018, JGRA, 123, 883
Mutch, T. A. 1980, JGR, 85, 7573
Newman, M., Schubert, G., Kliore, A. J., & Patel, I. R. 1984, JAtS, 41, 1901
Pätzold, M., Häusler, B., Bird, M. K., et al. 2007, Natur, 450, 657
Pätzold, M., Neubauer, F. M., Carone, L., et al. 2004, ESA SP-1240, Mars Express: the Scientific Payload (Noordwijk: ESA), 141
Pätzold, M., Tellmann, S., Andert, L., et al. 2009, ESA SP-1291: Mars Express: the Scientific Investigations (Noordwijk: ESA), 217
Schunk, R. W., & Nagy, A. F. 2009, Ionospheres (2nd ed.; New York: Cambridge Univ. Press)
Shinagawa, H., Kim, J., Nagy, A. F., & Cravens, T. E. 1991, JGR, 96, 11083
Withers, P., Felici, M., Flynn, C., & Vogt, M. F. 2020, PSJ, 1, 14
Withers, P., Fillingim, M. O., Lillis, R. J., et al. 2012, JGR, 117, A12307
Withers, P., Weiner, S., & Ferreri, N. R. 2015, EP&S, 67, 194
Woo, R., Armstrong, J. W., & Kliore, A. J. 1982, Icar, 52, 335
Woo, R., & Kliore, A. J. 1991, JGR, 96, 11073
Woo, R., Sjogren, W. L., Luhmann, J. G., Kliore, A. J., & Brace, L. H. 1989, JGR, 94, 1473
Zhang, M. H. G., Luhmann, J. G., & Kliore, A. J. 1990, JGR, 95, 17095